Evidence for a Northern Hemispheric trigger of the 100,000-y glacial cyclicity

Maayan Yehudai[a,b,1,2], Joohee Kim[a,b], Leopoldo D. Pena[c], Maria Jaume-Seguí[a,c], Karla P. Knudson[a], Louise Bolge[a], Alberto Malinverno[a,b], Torsten Bickert[d], and Steven L. Goldstein[a,b,2]

[a]Lamont-Doherty Earth Observatory, Columbia University, Palisades, NY 10964; [b]Department of Earth and Environmental Sciences, Columbia University, New York, NY 10027; [c]Department of Earth and Ocean Dynamics, University of Barcelona, 08028 Barcelona, Spain; and [d]MARUM–Center for Marine Environmental Sciences, University of Bremen, D-28359 Bremen, Germany

Edited by Michael L. Bender, Princeton University, Princeton, NJ, and approved September 3, 2021 (received for review September 28, 2020)

The causes of the Mid-Pleistocene Transition, the shift from ∼41-ky to 100-ky interglacial–glacial cycles and more intense ice ages, remain intensely debated, as this fundamental change occurred between ∼1,250 and 650 ka without substantial changes in astronomical climate forcings. Recent studies disagree about the relative importance of events and processes in the Northern and Southern Hemispheres, as well as whether the shift occurred gradually over several interglacial–glacial cycles or abruptly at ∼900 ka. We address these issues using a north-to-south reconstruction of the Atlantic arm of the global meridional overturning ocean circulation, a primary means for distributing heat around the globe, using neodymium (Nd) isotopes. Results reveal a period of intense erosion affecting the cratonic shields surrounding the North Atlantic between Marine Isotope Stages (MIS) 27 and 25 (∼980 and 950 ka), reflected by unusually low Nd isotope ratios in deep North Atlantic seawater. This episode preceded a major ocean circulation weakening between MIS 25 and 21 (950 and 860 ka) that coincided with the first ∼100-ky-long interglacial–glacial onset of Northern Hemisphere glaciation at around 2.4 to 2.8 Ma. The data point to a Northern Hemisphere–sourced initiation for the transition, possibly induced through regolith loss and increased exposure of the crystalline bedrock, which would lead to increased friction, enabling larger ice sheets that are characteristic of the 100-ky interglacial–glacial cycles.

Mid-Pleistocene Transition | Nd isotopes | paleocirculation | regolith hypothesis | AMOC structure

Earth's climate changed fundamentally between ∼1,250 and 650 ka, when the dominant glacial–interglacial variability shifted from ∼41- to ∼100-ky cycles and more intense glacials (1). The absence of significant changes in the Milankovitch astronomical climate forcings during this Mid-Pleistocene Transition (MPT) means that the primary climatic shifts occurred through nonlinear responses within the ocean–atmosphere–cryosphere system (e.g., ref. 2). While contributing events occurred in both the Northern (3–7) and Southern Hemispheres (8–12), the question of whether the cyclicity shift was driven primarily from the north or the south remains a major unresolved controversy. Some studies attribute the shift to long-term processes that occurred over several glacial cycles (e.g., refs. 1, 3, 4, 13, and 14), while others center the transition between Marine Isotope Stages (MIS) 24 and 22 (∼930 to ∼870 ka) and characterize the MPT as abrupt ("the 900-ka event"; refs. 8 and 11). Proposed drivers include long-term sea-surface and deep-water cooling (3, 4, 8), Southern and/or Northern Hemispheric sea-ice expansion (9, 15), decreased atmospheric CO_2 (12, 16, 17), increased ice-sheet stability (1, 14), and changes in the Atlantic meridional overturning ocean circulation, or AMOC. Given these disagreements and the large number of possible drivers, it is critical to constrain the timing, duration, and locations of the major events and processes that led to this profound climate-cycle shift and the dominance of 100-ky interglacial–glacial cycles.

Coeval changes in CO_2 and continental ice-sheet dynamics are tightly linked to changes in the AMOC (7, 10, 11, 18–20), and in particular the southward transport of past analogs of present-day North Atlantic Deep Water (NADW, henceforth termed "northern-sourced water," NSW, when referring to the past). In the modern ocean NSW formation occurs due to wind stresses that transport equatorial surface warm waters toward higher latitudes, which in turn causes evaporation and cooling that generates density gradients and eventually the sinking of cold and salty waters in the North Atlantic. This deep water mass can be traced all the way to the southern latitudes and into other oceans (20). This meridional prominence of NSW in the Atlantic basin has been shown to wane during glacials and wax during interglacials (e.g., refs. 7 and 20–22). Whether these glacial–interglacial structural changes are also reflected in the southward fluxes of NSW is a matter of debate, and although the availability of tracer data has increased over the past decade, there is currently no ocean circulation scenario that agrees with all the available data and models (23). While some geochemical evidence and modeling studies point to sustained NSW cell activity, for example during the last glacial maximum

Significance

Causes of the Mid-Pleistocene Transition (MPT) from 41- to 100-ky interglacial–glacial cyclicity are debated because it occurred without changes in solar forcing, thus indicating internal climatic drivers. This study reconstructs the deep Atlantic Ocean water-mass structure through the MPT using neodymium isotopes and distinguishes Northern and Southern Hemisphere precursors. North Atlantic results document changes in glacial erosion/weathering preceding the cyclicity shift, including a major erosional episode just before a global ocean circulation weakening between ∽950–860 ka. The findings indicate changes in Northern Hemispheric ice sheets prior to that weakening were central in shaping the cyclicity shift and the post-MPT glacial climate, whereby removal of weathered material exposed crystalline bedrock, resulting in increased bedrock–ice friction that facilitated larger ice sheets.

Author contributions: L.D.P. and S.L.G. designed research; M.Y., J.K., L.D.P., M.J.-S., K.P.K., L.B., T.B., and S.L.G. performed research; L.B. and A.M. contributed new reagents/analytic tools; M.Y., J.K., M.J.-S., and L.B. analyzed data; and M.Y. and S.L.G. wrote the paper.

The authors declare no competing interest.

This article is a PNAS Direct Submission.

[1]Present address: Department of Climate Geochemistry, Max Planck Institute for Chemistry, 55128 Mainz, Germany.

[2]To whom correspondence may be addressed. Email: my2430@columbia.edu or steveg@ldeo.columbia.edu.

This article contains supporting information online at http://www.pnas.org/lookup/suppl/doi:10.1073/pnas.2020260118/-/DCSupplemental.

Published November 8, 2021.

(e.g., refs. 24 and 25), others indicate shoaling and/or weakened strength of NSW southward transport over the Pleistocene glacials (20, 21, 26–28). Nevertheless, Atlantic Ocean deep water-mass meridional geometry reconstructions can help to decipher the timing and source locations for events and processes that preceded and thus likely impacted the MPT.

Pena and Goldstein (7) showed using Nd isotopes that the water mass structure of the AMOC in the southeast Atlantic changed significantly between MIS 25 and 21 (~950 and 860 ka) compared to previous interglacial–glacial cycles. The previous cycles lasted ~41 ky with relatively small differences in the signature of NSW between interglacial and glacial εNd values. They noted that the transition from MIS 25 to 24 was characterized by a significant weakening of the NSW signal to levels more typical of post-MPT glacials. This weakened NSW signal persisted through interglacial MIS 23 and glacial MIS 22, with recovery toward stronger NSW signatures only occurring at MIS 21. They also observed that MIS 23 is the only known interglacial in which the NSW εNd signature did not strengthen. MIS 25 to 21 also marked the first 100-ky-long interval where the AMOC structure was similar to post-MPT glacials, and they termed it the "MPT ocean circulation crisis." The importance of this time interval was recognized previously as it includes the 900-ka event. However, the Pena and Goldstein data (7) were limited to the far South Atlantic (Ocean Drilling Program [ODP] Sites 1088 and 1090, recovered from the upper and lower present-day boundaries of NADW; *SI Appendix*, Fig. S1) and did not address the extent of the AMOC-structure changes throughout the rest of the Atlantic basin over this interval. Here we term this same time interval between MIS 25 and 21 the "MPT-AMOC disruption" (with no implications in this study for changes in the AMOC flux strength), which our data, as described below, show can be observed throughout the Atlantic basin. The term "disruption" is used to describe the stark change in the ocean water mass structure and its timescale (lasting through MIS 25 to 21) compared to the previous ~0.5 Ma in our record.

The current study uses Nd-isotope ratios in Fe-Mn–encrusted foraminifera and fish debris in dated deep sea cores along a north–south Atlantic transect (Fig. 1 and *SI Appendix*, Fig. S1), representing the coeval seawater at each site through time, to trace changes in the AMOC water-mass structure through the MPT interval (*SI Appendix*, Fig. S2). The results yield insights into events that preceded the shift to ~100-ky cycles, reflecting changes in the Northern Hemisphere ice sheets that likely initiated the MPT-AMOC disruption and resulted afterward in longer and more stable glacial periods.

The Meridional εNd Transect Reflects Past Atlantic Ocean Deep Water-Mass Structure

Nd isotope ratios, presented as $^{143}Nd/^{144}Nd$ or εNd values, vary in rocks and waters as a result of radioactive α-decay of ^{147}Sm to ^{143}Nd (half-life = 106 Gy) and the preference of Nd over Sm to enter the liquid phase during melting of Earth's mantle. This has resulted in the continents having low Sm/Nd and $^{143}Nd/^{144}Nd$ ratios compared with the mantle. εNd is the deviation, in parts per 10,000, of the $^{143}Nd/^{144}Nd$ ratio of a sample from the value of chondritic meteorites, often called the Chondritic Uniform Reservoir, or CHUR, taken to represent the average composition of the solar system and the silicate Earth, thus $\varepsilon_{Nd} = \left[\frac{^{143}Nd/^{144}Nd_{sample}}{^{143}Nd/^{144}Nd_{CHUR}} - 1\right] \times 10^4$. This study references the εNd values to an estimated average chondrite value of $^{143}Nd/^{144}Nd = 0.512638$ (29). Mantle-derived rocks and young continental rocks have positive εNd values, whereas older continental rocks have negative εNd values, becoming systematically more negative with increasing crustal age.

The ocean residence time of Nd has been estimated to be ~500 to 1,000 y, shorter than or similar to the ocean mixing time (30, 31); thus, both Nd concentrations and εNd are inhomogeneous throughout the deep ocean. In the present day εNd has been shown to trace the movement of the major deep ocean water masses (a more comprehensive explanation of Nd isotopes in the oceans is given in *SI Appendix*, section 1). Over the past ~2 Ma the evidence indicates that the North Atlantic and North Pacific deep water mass end-members have sustained distinctive εNd values of about −14 vs. ~−4, respectively (*SI Appendix*, Fig. S3), and temporal changes at in-between locations can be used to trace changes in the water-mass structure (32–37). For Nd isotopes to robustly trace past changes in the water-mass structure at locations in between the end-members, εNd values should show systematic geographic gradients. At each site in the Atlantic and at each point in time a weakened southward NSW signature and an increased northward signature of southern-sourced water (SSW) would be reflected by higher (more Pacific-like) εNd values, and, likewise, increased dominance of NSW would be indicated by lower εNd values (7). These conditions are borne out by the data (Fig. 1 and *SI Appendix*, Fig. S2).

Comparison of the εNd records in our Atlantic transect (Fig. 1 and *SI Appendix*, Fig. S2) shows that they trace the temporal variability of the meridional AMOC structure, rather than the effects of sediment Nd exchange or Nd contributions from regional sources along the meridional water-mass transport paths (35, 38, 39), for several reasons. First, as expected for glacial–interglacial AMOC changes (21), glacial εNd values are nearly always more positive than neighboring interglacial values. There are two exceptions, both significant. One is a critical event during MIS 27 to 25 in the North Atlantic Deep Sea Drilling Project (DSDP) Site 607 (*SI Appendix*, Fig. S1) to be further discussed below. The other is the observation by Pena and Goldstein (7) that recognized the MPT-AMOC disruption in South Atlantic Sites 1088 and 1090, whereby MIS 23 does not show more negative εNd than bracketing glacials MIS 24 and MIS 22 (*SI Appendix*, Fig. S2). Second, at all locations and times the εNd values are more negative in samples expected to have higher NSW. That is, the north-to-south NSW–SSW gradients expected from AMOC mixing relationships are maintained throughout the record. The εNd values in closely spaced Equatorial ODP Sites 929 (40) and 926 (*SI Appendix*, Fig. S1) provide further evidence that the data express the AMOC structure through time. Site 929 is deeper (4,356 vs. 3,599 m) and consistently records more positive εNd values (*SI Appendix*, Fig. S2*A*), indicating greater deep-SSW influence, as expected from its greater depth, even though it is located slightly farther north (6°N vs. 3°N; *SI Appendix*, Fig. S1). Third, during interglacial maxima the εNd values at the North Atlantic Site 607 remain close to present-day NADW (~−13.5), both before and after the MPT-AMOC disruption (Fig. 1*D* and *SI Appendix*, Fig. S2*A*), consistent with previous studies showing that the NSW range during interglacials has remained similar since the mid-Pleistocene (refs. 7, 41 and 42, *SI Appendix*, Fig. S3, and see Fig. 3). Fourth, εNd values through the Atlantic transect remain between the North Atlantic and North Pacific global end-members at all times. Fifth, εNd in all the cores shows negative covariations with benthic $\delta^{13}C$ (*SI Appendix*, Figs. S4 and S5), expected if these proxies reflect glacial–interglacial AMOC changes (that is, excluding MIS-27 to MIS-25 data, discussed in more detail below). All these observations, taken together, provide strong evidence that the εNd data from all these cores reflect the AMOC structure. While a clear quantitative framework for accurately estimating the end-member mixing proportions or AMOC vigor is not yet available (for example, mixing depends on concentrations as well as isotope ratios, and Nd concentrations of the end-

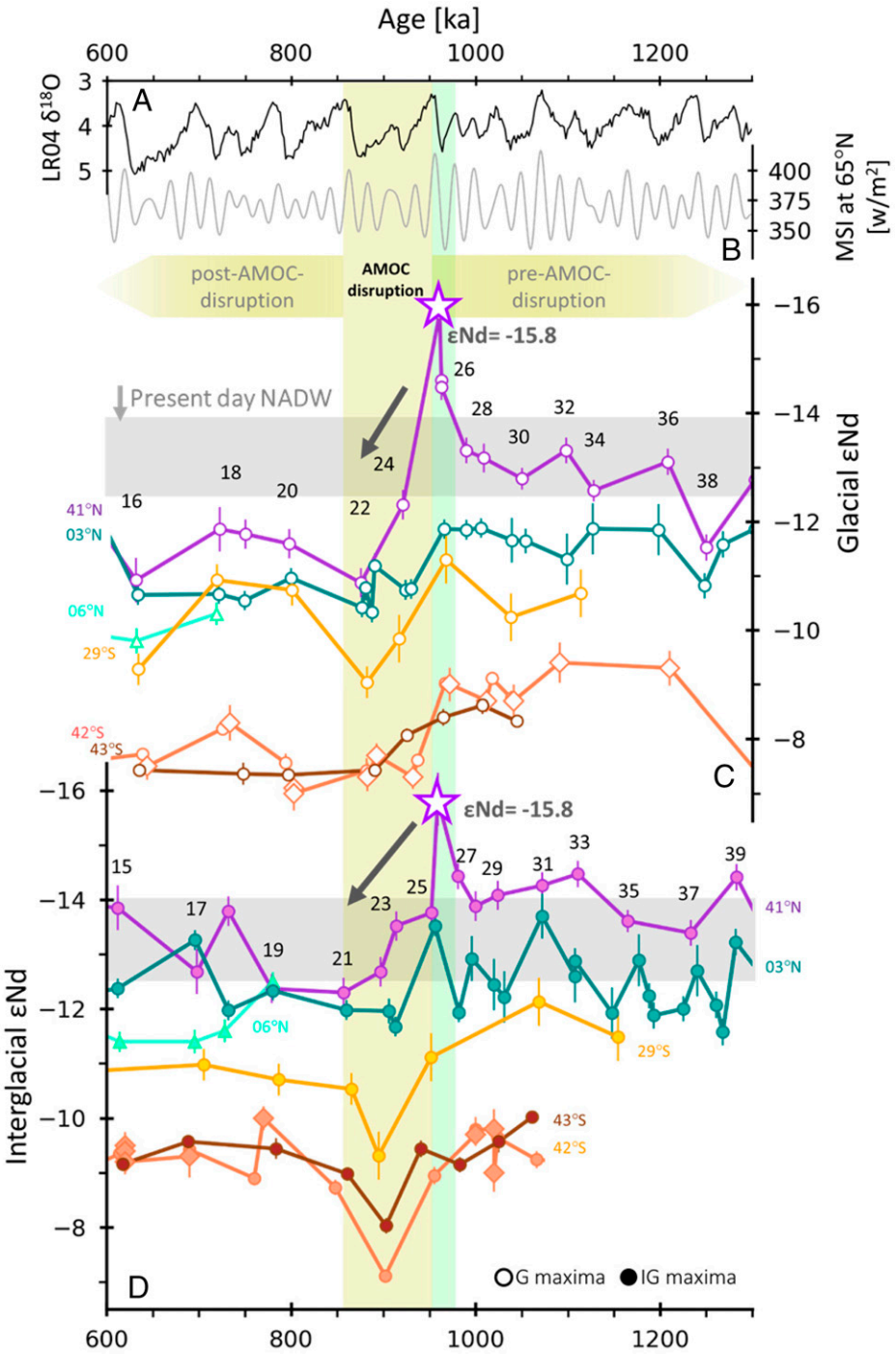

Fig. 1. Comparison of glacial and interglacial maxima εNd for the meridional transect. The time series is divided into three time windows: pre-AMOC-disruption refers to MIS 39 to 25 (~1,260 to 950 ka), MPT-AMOC disruption to MIS 25 to 21 (950 to 860 ka), and post-AMOC-disruption to MIS 21 to 15 (~860 to 600 ka). Open symbols are glacial maxima and solid symbols are interglacial maxima. (*A*) LR04 benthic $\delta^{18}O$ stack (78). (*B*) Mean summer insolation (MSI) at 65°N. (*C*) Glacial maxima εNd and (*D*) interglacial maxima εNd. Data are from DSDP Site 607 (violet; refs. 22 and 41), ODP Site 926 (blue; ref. 77), and previously published data from ODP Sites 1267 (yellow; ref. 10), 1088 (dark orange; diamonds represent ref. 83 and circles represent ref. 7) and 1090 (7). The shaded vertical green band highlights the MPT-AMOC disruption and the horizontal gray bands represent the present-day NADW εNd value (47). The interval between MIS 28 and 24 in *C* and MIS 27 and 25 in *D* in North Atlantic Site 607 represents the MIS-27-to-25 εNd excursion (bright green vertical shaded band); the purple star represents a negative εNd excursion within MIS 26 that includes ice-rafted detritus (*SI Appendix*, Fig. S7), reflecting breakdown of the Northern Hemisphere ice sheet prior to the MPT-AMOC disruption.

members through time are not well-constrained), the meridional relationships between these core records strongly support the utility of εNd as a measure of the impact/dominance of the North Atlantic and Pacific end-members at intermediate locations through time that can be compared to other climatic records. The observed relationships are consistent with interglacial–glacial changes in the AMOC structure, but they are unexpected for virtually any other scenario, for example

where Nd isotopes are impacted at a site by regional continental or sea-floor sediment sources (*SI Appendix*, section 2 and refs. 35, 38, 43, and 44).

The Deep North Atlantic Leading up to the ~100-ky World

The new transect reveals the Atlantic deep water-mass structure during the lead-up to the MPT. All sites show smaller glacial–interglacial εNd variability prior to the MPT-AMOC disruption (during MIS 39 to 25, ~1,280 to 950 ka) compared to afterward (MIS 21 to 15, ~860 to 610 ka). That is, glacial–interglacial εNd differences are greater in the 100-ky world, with glacials showing more positive εNd values (Fig. 1 and *SI Appendix*, Fig. S6 and Table S6), indicating a weakened NSW/stronger Pacific signature throughout the Atlantic during glacials following the MPT-AMOC disruption. Between MIS 39 and 26 (1,280 to 965 ka) at North Atlantic Site 607, interglacial εNd values remain close to the present-day NADW value, indicating similar interglacial conditions throughout, whereas glacial εNd are more variable (Fig. 2 and *SI Appendix*, Fig. S6). MIS 26 displays the most negative glacial maximum εNd value in the entire studied time interval and documents an unusually strong contribution of Nd from the surrounding continental cratonic shield regions to the North Atlantic. This observation is unique for Site 607 and is not observed at Site 926 further downstream (*SI Appendix*, Fig. S7 *F–J*).

Moreover, between MIS 27 and 25 (~980 to 950 ka), Site 607 data document a striking deviation from the characteristic glacial–interglacial εNd patterns (Fig. 2). While glacial maxima show more positive εNd values than the bracketing interglacials in all other known cases in the North Atlantic, as already noted, the MIS-26 glacial maximum shows more negative εNd values (−14.6) than interglacials MIS 25 (−13.4) and MIS 27 (−14.4) (Figs. 1 and 2 and *SI Appendix*, Fig. S2). In addition, MIS 26 is the only glacial maximum value that is more negative than present-day (interglacial) NADW (εNd ~−13.5). Between MIS 26 and MIS 25 the negative εNd value reaches −15.8 (Fig. 2) in a sample containing ice-rafted-detritus (IRD; *SI Appendix*, Fig. S8). In order to evaluate whether this value falls within expectations from the data leading up to it or is exceptional, we performed a statistical analysis of the predicted variability of the MIS-26 excursion data compared to the trends shown by the data from the previous glacial maxima and interglacial maxima (*SI Appendix*, Fig. S7 and section 2). When viewed as part of the sequence of data at Site 607 approaching the 900-ka event, this extreme negative εNd value (marked with a star in all figures) falls outside of the 95% prediction band for both the glacial and interglacial data. This means that the εNd value measured for this point in time is inconsistent with both the trends shown by the glacial maxima and the interglacial maxima, and therefore it represents an exceptional event. While the εNd-benthic $\delta^{13}C$ data in general show a negative glacial–interglacial covariation, which is consistent with increased SSW during glacials (*SI Appendix*, Figs. S4 and S5), this data point falls outside of the εNd-benthic $\delta^{13}C$ covariation, providing further evidence that it is exceptional.

The MIS-27-to-25 "εNd excursion" is followed by the first ~100-ky interglacial–glacial cycle during MIS 25 to MIS 21, which includes the MPT-AMOC disruption, shown by our Atlantic transect to be basin-wide (*SI Appendix*, Fig. S2*B*), and thus confirming its global impact. The new data presented in the transect allow for a detailed characterization of the disruption throughout the Atlantic. For example, the εNd shifts at Sites 607 and 926, in the North and Equatorial Atlantic, between MIS 25 and MIS 22, are larger than the shifts at the southern sites where the MPT-AMOC disruption was documented (~3 versus ~2 εNd units, respectively; *SI Appendix*, Fig. S2*B* and ref. 7). Between MIS 24 and MIS 22 the North and

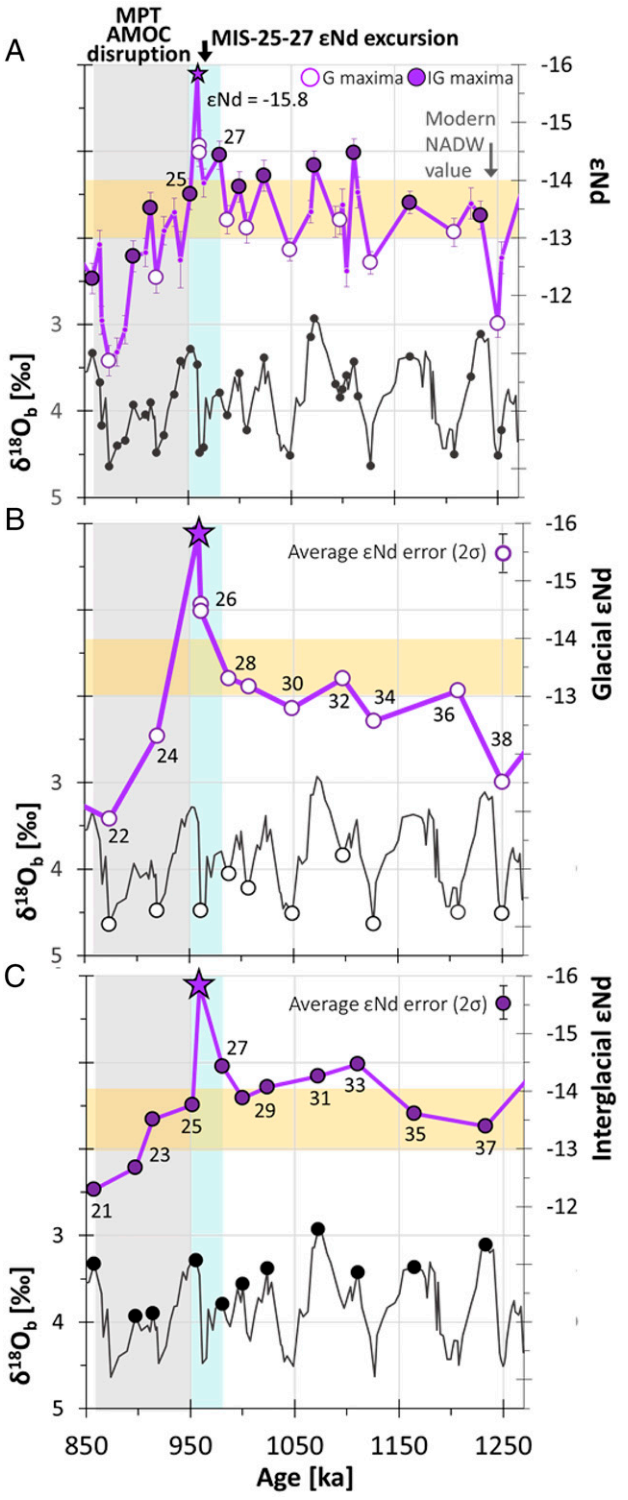

Fig. 2. North Atlantic εNd record approaching and through the MPT-AMOC disruption. (*A*) LR04 benthic $\delta^{18}O$ data (78) and εNd from DSDP Site 607. (*B*) The 607 glacial maxima and (*C*) 607 interglacial maxima εNd are shown separately. The yellow horizontal band represents the range of present-day NADW εNd values. The shaded gray band marks the MPT-AMOC disruption interval (7), showing high εNd values between MIS 25 and 21. The blue vertical band marks the MIS-27-to-25 εNd excursion that immediately preceded the MPT-AMOC disruption. The MIS-26 glacial maximum εNd value is more negative than the adjacent MIS-27 and MIS-25 interglacial values, which is unique to the North Atlantic record. The star plotted in all frames represents the highly negative εNd value within MIS 26.

Equatorial Atlantic data record the shift, characteristic of the 100-ky world, to stronger Pacific-like glacial εNd signatures.

Possible mechanistic explanations for the unusually negative εNd values in the deep North Atlantic during MIS 27 to 25 are increased weathering of the surrounding continental cratons or changes in the ocean circulation that creates NSW. The circulation mechanism would require both changes in the proportions of different water masses contributing to NSW (that is, Labrador versus Nordic or Greenland seas) and a modified North Atlantic circulation structure (18, 45). Considering NADW precursors, only shallow Baffin Bay water shows appropriately negative εNd values in the present day (to ∼−26; ref. 46), which are quickly diluted in the Labrador Sea, separating Baffin Bay from the deep North Atlantic, such that εNd of Labrador Sea water is ∼ −14, already similar to NADW, while εNd values more negative than −15 are neither observed south of ∼51°N nor deeper than ∼400 m (46, 47). Thus, we find a circulation mechanism to be unlikely, as it would require a means to transform Baffin Bay water from a shallow buoyant water mass on the Atlantic periphery to a water mass that impacts the main Atlantic basin at depth. The circulation scenario also conflicts with till-deposit-based geochemical evidence for increased presence of marine cold-based ice in the Baffin Bay–Labrador Sea region during glacials younger than ∼1.2 Ma. The presence of cold-based ice would dampen circulation during glacials in this region (18, 48). A simpler explanation is a change in cratonic weathering/erosion by ice sheets, which could affect εNd values of NSW precursor water masses and facilitate addition of Nd with negative εNd values to the deep Atlantic (49, 50). While these considerations do not preclude changes in the circulation of the NADW precursors during MIS 27 to 25, they do indicate intense cratonic weathering/erosion by the ice sheet as the cause of the negative MIS-26 εNd values in the deep North Atlantic, which is further buttressed by the observation of IRD in Site 607 (*SI Appendix*, Fig. S8).

Our observations thus point to intense glacial cratonic erosion during MIS 27 to 25, evidenced by the IRD (*SI Appendix*, Fig. S8) and signifying oceanic release of icebergs (51). These observations are consistent with the "regolith hypothesis" (1), which posits that since the onset of the Northern Hemisphere glaciation, soil and sedimentary rock removal from the continents, and the exposure of crystalline bedrock, led to a higher frictional coefficient between the ice sheets and the surface rock upon which ice sheets migrated (1). The increased friction would facilitate thicker ice sheets, which in turn would respond nonlinearly to Milankovitch orbital forcings, leading to prolonged and more intense ice ages. While we do not rule out other explanations, we currently favor regolith loss as a viable mechanism that could lead to our observations in the North Atlantic.

Additional longer-term evidence for increased cratonic erosion/chemical weathering approaching the shift to 100-ky glacial cyclicity is given by the evolution of the long-lived radiogenic isotope systems Sr, Pb, and Hf in the oceans (Fig. 3). For example, seawater $^{87}Sr/^{86}Sr$ ratios are uniform throughout the oceans, with a residence time of ∼2 to 5 My (52–54), more than three orders of magnitude longer than the ocean mixing time. As a result, Sr isotope ratios in seawater are highly buffered and thus resistant to sudden changes. Through the Cenozoic Era there has been a general increase in marine Sr-isotopes ratios, reflecting inputs

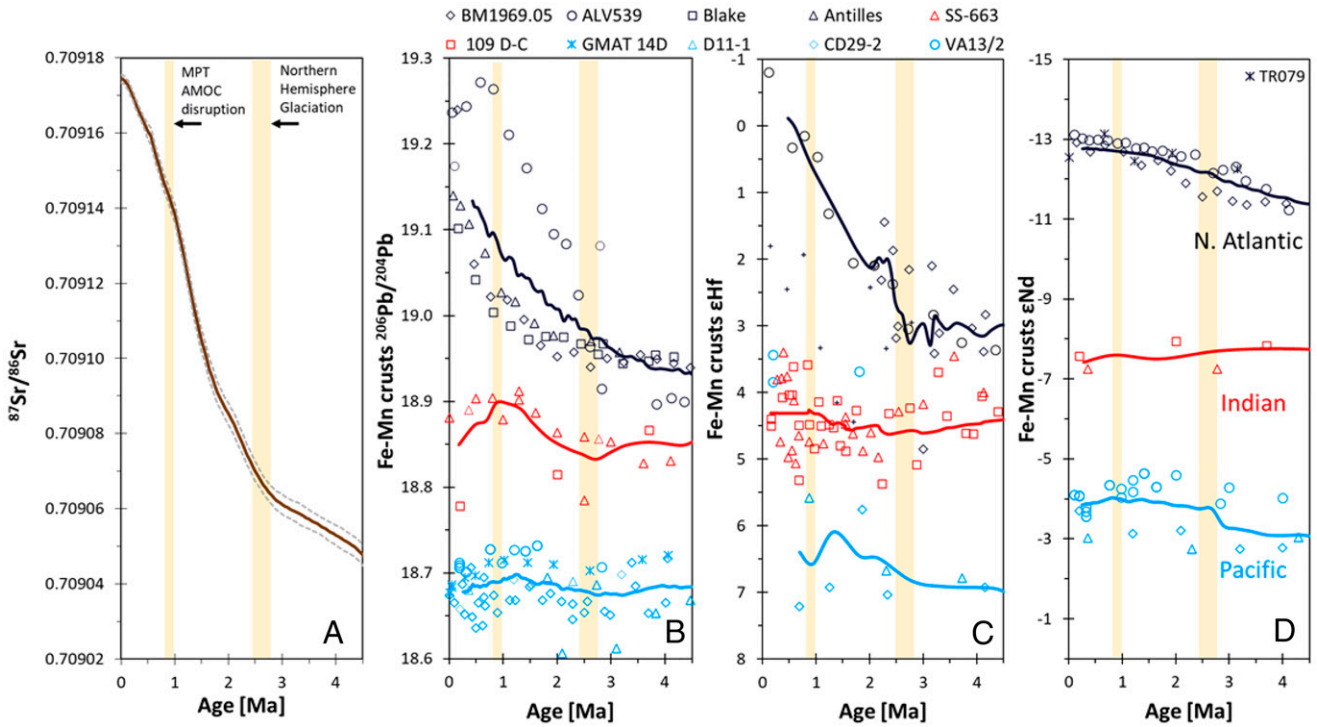

Fig. 3. Pleistocene (*A*) Sr, (*B*) Pb, (*C*) Hf, and (*D*) Nd isotope data in Fe-Mn crusts from different oceanic basins. (*A*) The LOWESS Sr-isotopes fit of the global synthesis version V4B 08 04 (80), courtesy of J. McArthur. The thin brown line shows the best estimate of the curve and light gray dashed lines show the 95% confidence limits. In *B*, *C*, and *D* the Atlantic, Indian, and Pacific basins are marked with black, red, and blue, respectively. The Fe-Mn crusts data are marked as follows. Atlantic: BM1969.05, black diamonds (58, 67); BM1969.05, black pluses (50); ALV539, black circles (61, 64, 66, 67); Blake, black squares (64); Antilles, black axes (64); Indian: 109D, red squares (58, 61); SS663, red triangles (58, 61); Pacific: VA13/2, blue circles (59–61, 65); D11-1, blue triangles (60, 62, 66); CD29-2, blue diamonds (60, 62, 66); and GMAT 14D, blue asterisks (81). Shaded yellow vertical bands mark the time intervals of the Northern Hemispheric (NH) glaciation and the 900-ka event or AMOC disruption. Increasing Sr and Pb isotope ratios and decreasing Hf isotope ratios in the Atlantic since intensification of NH glaciation between ∼2.5 to 2.8 Ma (82, 83), versus small changes for Indian and Pacific samples, indicate increased glacial erosion/weathering of NH cratons throughout the Pleistocene.

from increased global weathering of the continents (e.g., refs. 54–57). Through the warm Pliocene Epoch (5.3 to 2.8 Ma), ocean Sr isotope ratios remained nearly constant, but they started to increase during the early Pleistocene, coeval with the onset of the Northern Hemisphere glaciation (Fig. 3*A*). Pb and Hf isotope records of Fe-Mn crusts provide evidence that weathering of the Archean–Paleoproterozoic cratons surrounding the North Atlantic by the continental ice sheets are primary contributors to this increase (33, 50, 58–67). Hf and Pb have residence times shorter than or similar to Nd, and thus their isotope ratios, like εNd, vary within the different ocean basins. In the North Atlantic since ∼2.5 to 2.8 Ma, Pb and Hf isotope ratios show dramatic and persistent secular changes consistent with increased cratonic weathering (that is, increasing Pb and decreasing Hf isotope ratios), while the other basins remain constant or show much smaller changes (Fig. 3 *B* and *C*). These data thus clearly mark the Northern Hemisphere continents as a major source of increased erosion through the Pleistocene. Moreover, the secular trends toward a stronger cratonic fingerprint through time may indicate input of increasingly older continental crust. Nd isotopes in the North Atlantic Fe-Mn crusts show changes from εNd ∼−12 to ∼−13, also consistent with increased Pleistocene cratonic erosion (Fig. 3*D*). The Pb and Hf isotope patterns lend additional support to erosion of regolith in the cratonic areas through the early and mid Pleistocene, which would result in the increased exposure of fresh crystalline Archean–Paleoproterozoic bedrock.

Focusing in on the interval of ∼1.4 to 1.0 Ma approaching the MPT-AMOC disruption and the interglacial–glacial cyclicity shift, the marine Sr isotope record shows a particularly high rate of increase (Fig. 4*C* and *SI Appendix*, Fig. S9), consistent with an increased rate of ice-sheet-mediated continental weathering during this critical time interval. This would also bring in an increased amount of Nd with highly negative εNd values, which is most clearly seen in the MIS-27-to-25 εNd excursion at Site 607, and also in recently published data (68, 69) from ODP Site 1063 (33.41°N, 57.36°W, 4,584 m), a drift deposit on the deep Atlantic abyssal plain (*SI Appendix*, Fig. S1 and discussed below). We note that the timing of the shallowing of the Sr isotope trend at ∼1 Ma is not well-constrained, and in Fig. 4 it appears to occur prior to MIS 27. However, the lower density of available data between ∼1.4 and 1.1 Ma, compared to older and younger ages, and the relatively high spread of the data at ∼1 Ma (Fig. 4) makes it difficult to precisely constrain the timing of the shallowing of the slope, as seen from other studies that place it at ∼1 Ma (Fig. 3, *SI Appendix*, Fig. S9, and ref. 70). Moreover, the long marine residence time of Sr (2 to 5 My, three orders of magnitude longer than the ocean mixing time) makes it insensitive to any short-term perturbations, unlike Nd isotopes, which record ocean changes on subglacial–interglacial timescales. This means that even an intense short-term εNd excursion like the one during MIS 27 to 25 is unlikely to be observable in the Sr isotope record. In summary, Sr isotopes can only record long-term trends while Nd isotopes can record short-term events. Although it is unclear whether the shallowing of the trend shown by marine Sr isotopes overlaps with the MIS-27-to-25 event, its steep slope between ∼1.4 and 1.0 Ma points to intense continental weathering. In addition, the Hf and Pb isotopes point to the Northern Hemisphere cratons as the locus of increased weathering throughout the Pleistocene. Together, these observations from the Sr, Hf, and Pb isotopes are consistent with the εNd data for Site 607 during the MIS-27-to-25 εNd excursion that directly preceded the shift to 100-ky interglacial–glacial cycles.

While the Sr isotope ratios indicate increasingly intense continental cratonic ice-sheet erosion between ∼1.4 and 1.0 Ma, the evidence from Nd isotopes in the North Atlantic Site 607 over the time interval approaching the MIS-27-to-25 event is

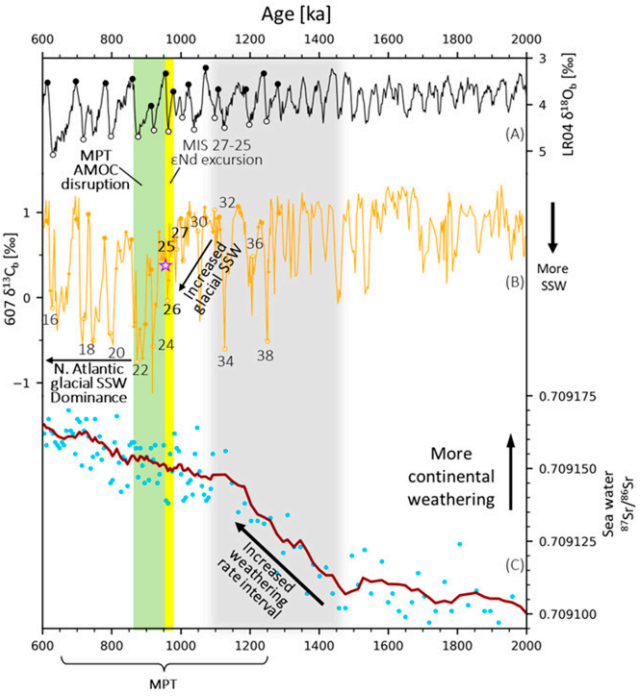

Fig. 4. Extended view of circulation and weathering proxies from the early Pleistocene. (*A*) LR04 benthic $\delta^{18}O$ stack (78) for stratigraphic reference, including the glacial (empty circles) and interglacial (full circles) minima and maxima of the studied interval. (*B*) Site 607 benthic $\delta^{13}C$ (45); filled (interglacial maxima) and open (glacial maxima) circles and small diamonds (transitional points) represent samples used for εNd analysis. The purple star represents the most negative εNd point during the MIS-27-to-25 εNd excursion (yellow vertical band), just before the MPT-AMOC disruption (green vertical band). (*C*) Seawater $^{87}Sr/^{86}Sr$ from DSDP Site 758 (84) smoothed data (over ∼40-ky window, dark red line), showing a steeper slope between ∼1,400 to 1,100 ka (gray vertical band), indicating increased continental weathering rates.

equivocal. Our linear regression analyses of all the seven glacial maxima data between MIS 38 and 26 in Site 607, and any combination of six of the data points, show statistically significant trends toward increasingly negative εNd values, consistent with increased continental erosion. However, if both MIS 38 and MIS 26 are excluded, the five remaining data points show no trend (Fig. 2*A* and *SI Appendix*, Fig. S7 and section 2). As already noted, MIS 26 in Site 607 remains significant as the only known instance where the glacial εNd value is more negative than the bracketing interglacials, and the regression analysis shows that the highly negative transitional data point between MIS 26 and 25 falls outside of the 95% prediction band for all the linear regression tests (*SI Appendix*, Fig. S7). Nevertheless, evidence for intense cratonic erosion during the latter part of this interval is shown in a recent study (68) of drift-deposit Site 1063 from the northwest Atlantic abyssal plain (*SI Appendix*, Fig. S1), which found that this site exhibits extremely negative εNd values throughout the late Pleistocene (*SI Appendix*, Fig. S10). The Site 1063 data are not consistent with the AMOC structure, as shown by the meridional transect (Fig. 1 and *SI Appendix*, Figs. S2 and S6). Rather, they reflect the input of Nd from the Canadian shield, eroded into the North Atlantic (68). εNd values at Site 1063 just prior to the MPT-AMOC disruption (between MIS 29 and MIS 25) are particularly negative compared to the rest of this site's record, reaching −26 during MIS 27 (*SI Appendix*, Fig. S10), signaling an exceptionally high cratonic contribution.

The glacial εNd values at Site 607 leading up to the MIS-27-to-25 negative εNd excursion, while slightly more positive than

the interglacial values, are still quite negative relative to the post MPT-AMOC disruption glacial values, and fall within the range of present-day NADW (Figs. 1 and 2). We suggest two mechanistic scenarios (Fig. 5) to explain this observation. One scenario attributes these negative glacial εNd values to the culmination of increased exposure of the underlying older cratonic continent as a consequence of regolith removal by the ice sheets (Figs. 3 and 5 *A*, *C*, and *D* and ref. 71). The second scenario would reflect shifting of the location of the Nd weathering source regions into the North Atlantic basin to areas where older cratonic regions are exposed, driven by the regolith removal and ice-sheet migration over the North American continent (Fig. 5*B*). Of course, the changes observed in the deep North Atlantic εNd values could be the result of a combination of both scenarios, and future studies may be able to distinguish between them, using combined observations from geochemistry and ice-sheet dynamics (32). In both scenarios, throughout the early Pleistocene, the more "slippery" regolith was gradually removed, exposing crystalline bedrock that was less slippery and much more resistant to erosion. The ice sheet in contact with crystalline bedrock would dominate the 100-ky world, where in addition the signal from glacial incursions of SSW (Fig. 5*D* and discussed below) overwhelmed any weathering signal at Site 607. This is also the case for the glacial εNd values at Site 1063 after MIS 25, which mostly overlap with Site 607, in contrast to interglacials and transitional intervals (*SI Appendix*, Fig. S10).

The AMOC Structure and the Onset of the 100-ky World

Although the Site 607 εNd values indicate increased cratonic weathering into the North Atlantic during the MIS-27-to-25 εNd excursion, ocean circulation changes, revealed by the benthic foraminiferal $\delta^{13}C$ record, indicate increasing SSW influence during the same time interval (Fig. 4*B*). This difference

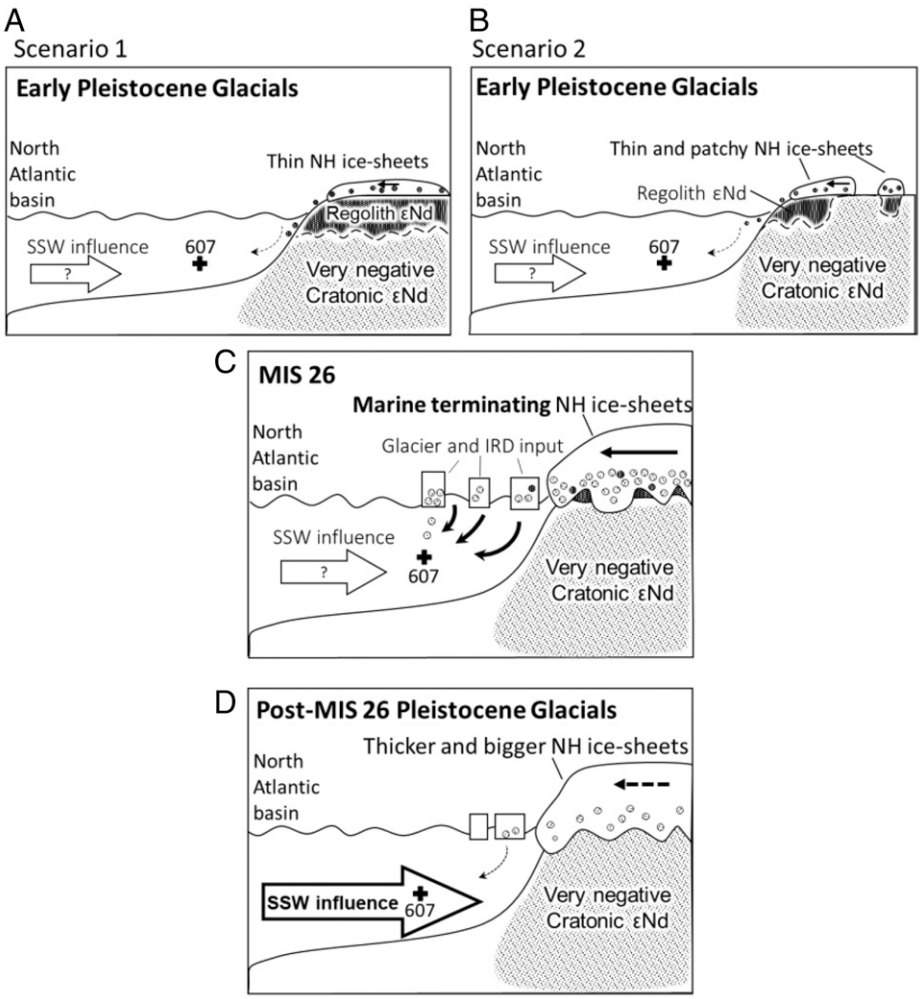

Fig. 5. A schematic speculative cartoon describing the different weathering scenarios that could explain the εNd data of the North Atlantic basin at Site 607. Scenario 1 (*A*) represents contributions of Nd to the North Atlantic basin during regolith removal where the regolith shows higher εNd than the underlying crystalline cratonic basement. In scenario 2 (*B*) the change in Nd isotopic input into the North Atlantic basin is due to the lateral migration of the source areas of the weathering products into areas with exposed older cratonic material, as the ice sheets evolved since the Northern Hemispheric Glaciation. In both cases, during the Early Pleistocene glacials (*A* and *B*) the low frictional coefficient between ice and weathered regolith material resulted in smaller and thinner ice sheets that may not have reached the subpolar coastal regions. Simultaneously, the strong influence of SSW in the deep North Atlantic basin, characteristic of post-MPT glacials, had not yet begun. (*C*) The increased exposure of fresh crystalline material supported thicker and more extensive marine-terminating ice sheets (1) and increased erosional efficiency. Right before the MPT-AMOC disruption, during the MIS-27-to-25 εNd excursion, these developments along with increased ice-mass loss due to the contact with the ocean allowed for major phase of regolith removal along with an increased flux of older continent containing lower εNd values. At the same time, the SSW impact moderately increased, as can be seen from the benthic $\delta^{13}C$ data at Site 607 (see Fig. 4*B*). (*D*) Following the MPT-AMOC disruption, εNd of the North Atlantic basin during glacials was strongly influenced by SSW that has overwhelmed the erosional signal.

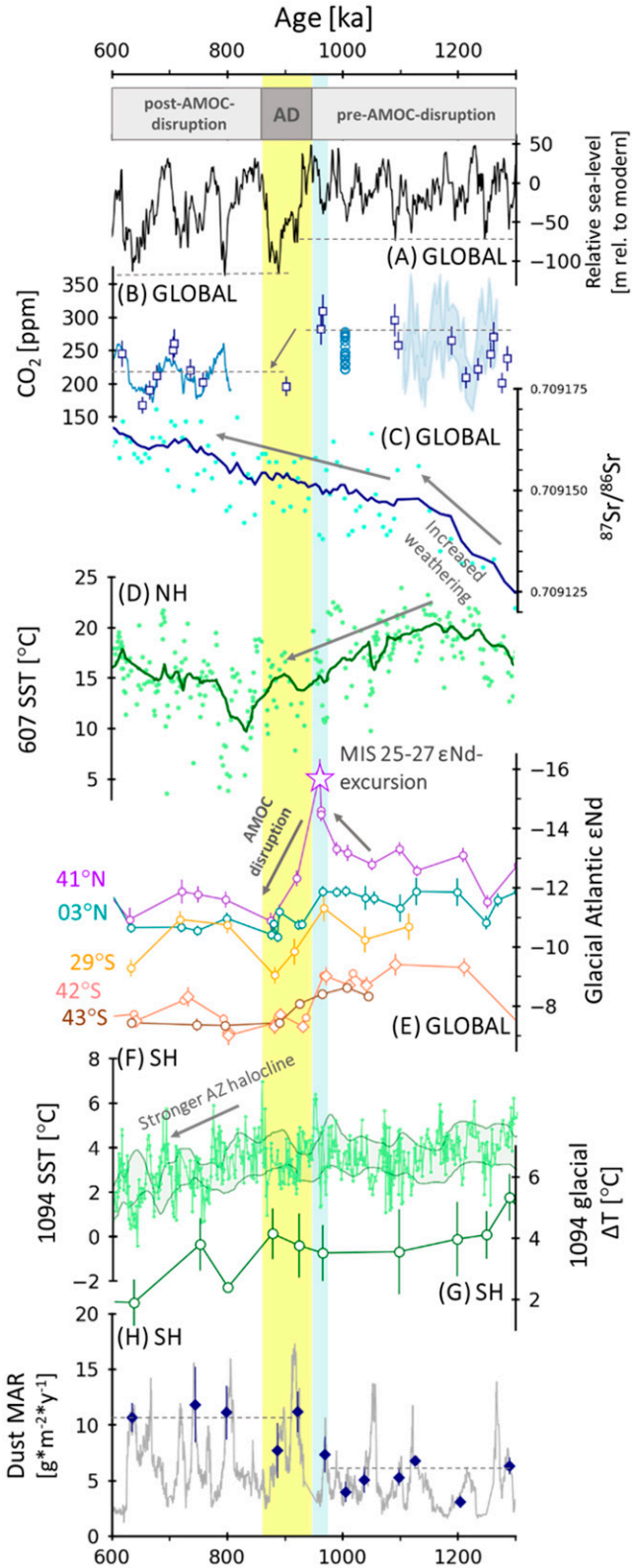

Fig. 6. Timing of global, Northern Hemisphere (NH), and Southern Hemisphere (SH) MPT-related changes. (*A*) Sea level changes (modified after ref. 8). Black dashed lines indicate the sea level/ice volume changes for glacial maxima before and after the MPT-AMOC disruption. (*B*) CO_2 changes from EPICA-DOME-C (blue line; ref. 85), Alan Hills (blue circles; ref. 86), and boron isotope data (shaded light blue and navy squares; refs. 12 and 17). The dashed lines indicate average CO_2 before and after the MPT-AMOC disruption. The arrow indicates the timing of the main CO_2 drop during the 900-ka event. (*C*) Global sea water $^{87}Sr/^{86}Sr$ ratios recorded at DSDP Site 758 (84). The arrows mark the increase in weathering rates over the pre-AMOC-disruption period (the change in slope is shown more distinctly in Figs. 3 and 4). The dark blue line represents smoothing over a ~40-ky window. (*D*) Sea surface temperatures (SST) from Site 607 (3, 87), showing decreasing SST prior to the 900-ka event. The dark green line represents smoothing over a ~23-ky window. (*E*) εNd of the transect for glacial maxima, including data from this study and published works (7, 22, 79, 88). The MIS-27-to-25 εNd excursion and effects of the MPT-AMOC disruption are clear in Site 607. (*F*) SST from the Antarctic Zone (AZ; ref. 11) Site 1094. The dark green line is as in *D* and shows a later occurring and a more gradual decrease in Southern Hemisphere SST. (*G*) SST and bottom water temperature gradients from Site 1094 (11). (*H*) Sub-Antarctic Zone iron-based dust flux (gray line; ref. 89). The blue diamonds represent binned averages of glacial iron flux maxima (90). The dashed lines represent average fluxes before and after the MPT-AMOC disruption. The vertical shaded yellow area represents the MPT-AMOC disruption, which represents a major change in the meridional Atlantic water-mass structure and a weakening of the NSW influence (abbreviated as AD; ref. 7). The shaded blue band represents the MIS-27-to-25 εNd excursion.

between evidence from the benthic $\delta^{13}C$ and from εNd further strengthens the interpretation that the MIS-27-to-25 εNd excursion represents an erosion/weathering event in the Northern Hemisphere cratons rather than a change in the water-mass structure. Following MIS 25, that is, during the MPT-AMOC disruption and afterward, the effect of increased SSW in the deep North Atlantic during glacials is apparent in both the benthic $\delta^{13}C$ and the εNd records (Figs. 1*C*, 4*B*, and 6*E* and *SI Appendix*, Figs. S2 and S4*A*). In other words, during the MPT-AMOC disruption and afterward, the glacial benthic $\delta^{13}C$ values of the deep North Atlantic are lower and εNd values are more positive. The inverse correlation between εNd and benthic $\delta^{13}C$, indicating a stronger SSW signal, is consistent with major glacial SSW incursions into the deep North Atlantic basin in the 100-ky world. We suggest that in the 100-ky world the domination of SSW in the deep North Atlantic overwhelmed the impact of cratonic weathering on the εNd values at Site 607 (Figs. 4*B* and 5 *C* and *F* and *SI Appendix*, Fig. S10). The more positive glacial εNd values after the MPT-AMOC disruption may have also been facilitated by lower cratonic weathering rates, as indicated by the shallowing of the slope of seawater $^{87}Sr/^{86}Sr$ ratios at ~1.0 Ma (Figs. 4*C* and 6 and *SI Appendix*, Fig. S9). The increased glacial SSW presence affected other parts of the North Atlantic basin as well, as seen from a comparison between Sites 607 and 1063 (*SI Appendix*, Fig. S10). While the interglacials and transitional intervals at Sites 1063 and 607 diverge after the MPT-AMOC disruption, the similarity of the glacial values at both sites further corroborates the glacial domination of SSW throughout the entire North Atlantic basin following MIS 26 (68).

Our data are consistent with previous suggestions that the MPT was the time when ice sheets reached a critical stability level that instigated major AMOC structure changes during glacials, as evidenced by the positive glacial εNd values observed in the deep North Atlantic at both Sites 607 and 1063 since MIS 26 (Figs. 1*B* and 2*A* and ref. 7). Approaching the cyclicity shift, the negative glacial εNd values during MIS 27 to 25 (*SI Appendix*, Fig. S10) and the presence of IRD within MIS 26 (*SI Appendix*, Fig. S7) are consistent with our preference for glacial erosion of the cratons and ice-sheet-driven regolith removal among possible explanations. We speculate that during the early Pleistocene the ice sheet was thin because it slid easily on the deformable regolith that was present on the continents beneath the ice. The resulting thinner ice sheets did not reach all the way to the subpolar coastal areas of the Northern Hemisphere continents. In this case, weathering products entered the ocean via rivers rather than glacier systems and icebergs.

Regolith removal resulted in exposure of crystalline bedrock, whereby the ice sheet became hard-bedded and the sliding coefficient decreased (that is, the ice sheet slid slower for a given driving stress). This resulted in a thicker ice sheet that advanced toward the ocean. The MIS-27-to-25 εNd excursion may represent a critical stage when Northern Hemisphere ice sheets finally became marine-terminating. This change in setting would have caused accelerated ice-mass loss, leading to increased freshwater contributions into the North Atlantic basin through calving and iceberg production (as evidenced by the IRD; *SI Appendix*, Fig. S7 and refs. 72 and 73). This would lead in turn to a basin-wide weakening of the NSW cell influence during the AMOC disruption. Then, as the ice sheet lost mass and the balance between snow accumulation, ice flow and ice-mass loss was regained, ice outflow would have decreased. Nevertheless, the permanent change in the bedrock (that is, the loss of regolith) would have left the ice sheet thicker than it was before, which allowed for the persistence of the 100-ky glacial–interglacial cycles. In summary, we suggest that the evolution of the ice sheets from those characteristic of the 41-ky world to those characteristic of the 100-ky world involved two transitions, an earlier one from soft-bedded to hard-bedded and a later one from terrestrial- to marine-terminating.

The observations from the North Atlantic (Fig. 2 and *SI Appendix*, Fig. S10) thus indicate that cratonic erosion by ice sheets played a major role in the MPT, leading to two critical events: a major erosional event reflected by the MIS-27-to-25 εNd excursion, followed by the MPT-AMOC disruption that included the 900-ka event, which in turn was followed by fundamental changes in the large-scale variability and temporal patterns of the global climate system (Fig. 6). Our results are consistent with previous studies showing ice-sheet expansion and thickening (1, 5), surface and bottom water gradual cooling (3, 14), freshening of the North Atlantic (74), and changes in the global weathering rate (1, 75) prior to the 900-ka event (Fig. 6 *C* and *D*).

Northern and Southern Hemispheric Processes That Led to the 900-ka Event

While this study focuses on events in the North Atlantic, the climate system is globally interconnected, and other recent studies point to linkages between Southern Hemisphere processes/events, the global carbon cycle, and the 900-ka event (e.g., Fig. 3 *F*–*H*). For example, enhanced glacial dustiness resulted in increased iron fertilization in the Southern Ocean (Fig. 6*H* and ref. 12), while decreased Southern Ocean ventilation increased the oceanic carbon storage capacity (Fig. 6 *F* and *G* and ref. 11). Together, these enabled pCO_2 drawdown, which facilitated larger ice sheets and contributed to the intensification of glacials. A recent study (10) emphasizes the tight coupling between changes in AMOC structure and the increased oceanic carbon-storage capacity in the Southern Ocean that facilitated CO_2 drawdown. These changes are directly associated with the 900-ka event. In the case of increased carbon storage (10) the direct relation to a weaker NSW influence throughout the Atlantic indicates a Northern Hemisphere cause, consistent with our data pointing to the Northern Hemisphere ice-sheet dynamics as a major driver for the shift. The AMOC structure changes that are revealed by the εNd data reflect the competing effects of SSW versus NSW, where the larger glacial standing volume of the high CO_2 content SSW would further amplify the glacial–interglacial atmospheric CO_2 fluctuations that are observed after the 900-ka event. Importantly, our Nd-isotope data, along with other patterns in the North Atlantic preceding the 900-ka event (Figs. 3 and 6), show that Northern Hemisphere changes temporally preceded these Southern Hemisphere shifts.

Summary

This study presents insights into the connections between the Northern Hemisphere ice-sheet activity and past AMOC structure fluctuations. Our north-to-south Atlantic reconstruction of the AMOC structure using Nd isotopes reveals the critical role of events and processes in the Northern Hemisphere in the lead up to the transition from ∼41- to 100-ky interglacial–glacial cycles. Erosion/weathering of the cratons surrounding the North Atlantic increased since the onset of Northern Hemisphere glaciation, as evidenced by the secular changes in marine Sr, Pb, and Hf isotopes (Fig. 3), with Sr isotopes indicating particularly accelerated rates of erosion/weathering during the interval of ∼1.4 to 1.0 Ma (Figs. 3 and 4 and *SI Appendix*, Fig. S7). During MIS 27 to 25 (∼980 to 950 ka) an extraordinarily intense phase of erosion/weathering is revealed by an εNd excursion to unusually negative values at North Atlantic DSDP Site 607, which included iceberg activity of marine-terminating ice sheets, as evidenced by IRD. The ensuing freshening of the North Atlantic led to the MPT AMOC disruption (7), the first intensified glacial cycle that lasted ∼100 ky (MIS 25 to 21, 950 to 860 ka). The 100-ky glacial cycles that have since dominated to the present day have been stabilized by the increased friction between the Northern Hemisphere continental ice sheets and the bedrock surface that likely resulted from the shedding of the regolith, as well as increased CO_2 storage capacity in the oceans.

Materials and Methods

The sediment core samples collected were gently sieved with deionized water to separate coarse fractions (>63 μm), which were then dried in a laboratory oven below 50 to 55 °C. For foraminifera samples, 20 to 50 mg of foraminifera were hand-picked from the >355-μm, >300-μm, and/or >250-μm fractions. For fish debris samples, at least 40 μg of fish debris were hand-picked. Foraminifera shells were gently crushed in order to open chambers, and any detrital materials observable under the microscope were manually removed. The samples then underwent ultrasonic agitations and resuspensions in Milli-Q water and methanol to further remove any remaining clay material. This process was repeated until the supernatant fluid became clear. The cleaned foraminifera samples were then dissolved by adding 0.5 mL of Milli-Q and 100 μL of concentrated acetic acid to the samples and through ultrasonication. Subsequent addition of 100 μL of concentrated acetic acid and multiple ultrasonications were repeated until the complete dissolution of the foraminifera fragments. The fish debris samples were cleaned using a procedure similar to that for the foraminifera for clay removal and were then dissolved in a 1:1 solution of 1 N nitric and 1 N hydrochloric acids. Next, the samples were processed through Tru-Spec column chemistry, to separate and collect rare earth elements, followed by Ln-Spec column chemistry to separate and collect Nd.

$^{143}Nd/^{144}Nd$ ratios were measured using the ThermoScientific Neptune Plus multicollector inductively coupled plasma mass spectrometer at the Lamont-Doherty Earth Observatory of Columbia University. Instrumental mass bias was corrected using an exponential mass fractionation law using $^{146}Nd/^{144}Nd = 0.7129$. $^{143}Nd/^{144}Nd$ values for samples were adjusted to a value for the JNdi standard of $^{143}Nd/^{144}Nd = 0.512115$ (76). All sample measurements were bracketed by standards to monitor instrumental drift and corrected accordingly. External reproducibility from routine runs of the JNdi standard ranged from ±11 to $\pm 21 \times 10^{-6}$ (2 SD) during multiple measurement sessions, returning external errors of ±0.21 to 0.40 εNd units (2 SD). In-run measurement precision was much better than the external reproducibility; however, if the internal precision was worse than external errors, internal errors are reported. The εNd data presented in this paper are listed in *SI Appendix*, Tables S1, S2, and S3 (10, 41, 77).

Data Availability. Nd isotopes for International Ocean Discovery Program Sites 607 (41) and 926 (77) have been deposited in EarthChem Data Library (https://doi.org/10.26022/IEDA/111576 and https://doi.org/10.26022/IEDA/111588, respectively).

ACKNOWLEDGMENTS. This study was primarily supported by NSF grant OCE-14-36079. S.L.G. also acknowledges support from the Storke Endowment of the Columbia University Department of Earth and Environmental Sciences. Samples were provided by the International Ocean Discovery Program, sponsored by the NSF and participating countries under management of Joint

Oceanographic Institutions. T. Fahey helped with sample preparation. We thank B. Hönisch, M. Raymo, H. Ford, L. Haynes, J. Farmer, G. Haug, A. Martínez-García, A. Hasenfratz, D. Hodell, J. McManus, C. Basak, Mordechai Stein, and J. Kingslake for discussions. S.L.G. thanks John McArthur for providing the LOWESS fit of the global Sr isotope stratigraphy data used in Fig. 3 and *SI Appendix*, Fig. S9. We particularly thank Alexander M. Piotrowski, Der-Chuen Lee, and John N. Christensen for their efforts to find the old Fe-Mn crusts data files that are no longer available on the journals' websites.

1. P. U. Clark *et al.*, The middle Pleistocene transition: Characteristics, mechanisms, and implications for long-term changes in atmospheric pCO2. *Quat. Sci. Rev.* **25**, 3150–3184 (2006).
2. P. Huybers, E. Tziperman, Integrated summer insolation forcing and 40, 000-year glacial cycles: The perspective from an ice-sheet/energy-balance model. *Paleoceanography* **23**, 1–18 (2008).
3. S. Sosdian, Y. Rosenthal, Deep-sea temperature and ice volume changes across the Pliocene-Pleistocene climate transitions. *Science* **325**, 306–310 (2009).
4. H. L. Ford, S. M. Sosdian, Y. Rosenthal, M. E. Raymo, Gradual and abrupt changes during the mid-Pleistocene transition. *Quat. Sci. Rev.* **148**, 222–233 (2016).
5. S. Kender *et al.*, Closure of the Bering Strait caused Mid-Pleistocene Transition cooling. *Nat. Commun.* **9**, 5386 (2018).
6. H. Detlef *et al.*, Sea ice dynamics across the Mid-Pleistocene transition in the Bering Sea. *Nat. Commun.* **9**, 941 (2018).
7. L. D. Pena, S. L. Goldstein, Thermohaline circulation crisis and impacts during the mid-Pleistocene transition. *Science* **345**, 318–322 (2014).
8. H. Elderfield *et al.*, Evolution of ocean temperature and ice volume through the mid-Pleistocene climate transition. *Science* **337**, 704–709 (2012).
9. C. H. Lear *et al.*, Breathing more deeply: Deep ocean carbon storage during the mid-Pleistocene climate transition. *Geology* **44**, 1035–1038 (2016).
10. J. R. Farmer *et al.*, Deep Atlantic Ocean carbon storage and the rise of 100,000-year glacial cycles. *Nat. Geosci.* **12**, 355–360 (2019).
11. A. P. Hasenfratz *et al.*, The residence time of Southern Ocean surface waters and the 100,000-year ice age cycle. *Science* **363**, 1080–1084 (2019).
12. T. B. Chalk *et al.*, Causes of ice age intensification across the mid-Pleistocene transition. *Proc. Natl. Acad. Sci. U.S.A.* **114**, 13114–13119 (2017).
13. E. L. McClymont, S. M. Sosdian, A. Rosell-Melé, Y. Rosenthal, Pleistocene sea-surface temperature evolution: Early cooling, delayed glacial intensification, and implications for the mid-Pleistocene climate transition. *Earth Sci. Rev.* **123**, 173–193 (2013).
14. C. W. Snyder, Evolution of global temperature over the past two million years. *Nature* **538**, 226–228 (2016).
15. H. Gildor, E. Tziperman, Sea ice as the glacial cycles' climate switch: Role of seasonal and orbital forcing. *Paleoceanography* **15**, 605–615 (2000).
16. M. E. Raymo, D. W. Oppo, W. Curry, The mid-Pleistocene climate transition: A deep sea carbon isotopic perspective. *Paleoceanography* **12**, 546–559 (1997).
17. B. Hönisch, N. G. Hemming, D. Archer, M. Siddall, J. F. McManus, Atmospheric carbon dioxide concentration across the mid-Pleistocene transition. *Science* **324**, 1551–1554 (2009).
18. M. E. Raymo *et al.*, Stability of North Atlantic water masses in face of pronounced climate variability during the Pleistocene. *Paleoceanography* **19**, 1–13 (2004).
19. N. J. Shackleton, J. Imbrie, M. A. Hall, Oxygen and carbon isotope record of East Pacific core V19-30: Implications for the formation of deep water in the late Pleistocene North Atlantic. *Earth Planet. Sci. Lett.* **65**, 233–244 (1983).
20. W. Broecker, The great ocean conveyor. *Oceanography* **4**, 79–89 (1991).
21. W. B. Curry, D. W. Oppo, Glacial water mass geometry and the distribution of δ13C of ΣCO2 in the western Atlantic Ocean. *Paleoceanography* **20**, 1–12 (2005).
22. J. Kim *et al.*, North Atlantic deep water during Pleistocene interglacials and glacials. *Quat. Sci. Rev.* **269**, 107146 (2021).
23. J. Lynch-Stieglitz, T. M. Marchitto, *Tracers of Past Ocean Circulation* (Elsevier Ltd., ed. 2, 2013).
24. S. Sherriff-Tadano, A. Abe-Ouchi, M. Yoshimori, A. Oka, W. Le Chan, Influence of glacial ice sheets on the Atlantic meridional overturning circulation through surface wind change. *Clim. Dyn.* **50**, 2881–2903 (2018).
25. J. F. McManus, R. Francois, J. M. Gherardi, L. D. Keigwin, S. Brown-Leger, Collapse and rapid resumption of Atlantic meridional circulation linked to deglacial climate changes. *Nature* **428**, 834–837 (2004).
26. J. F. Adkins, The role of deep ocean circulation in setting glacial climates. *Paleoceanography* **28**, 539–561 (2013).
27. N. L. Roberts, A. M. Piotrowski, J. F. McManus, L. D. Keigwin, Synchronous deglacial overturning and water mass source changes. *Science* **327**, 75–78 (2010).
28. J. Lynch-Stieglitz, *et al.*, Meridional overturning circulation in the South Atlantic at the last glacial maximum. *Geochem. Geophys. Geosyst.* **7**, 10.1029/2005GC001226 (2006).
29. S. B. Jacobsen, G. J. Wasserburg, Sm-Nd isotopic evolution of chondrites. *Earth Planet. Sci. Lett.* **50**, 139–155 (1980).
30. K. Tachikawa, C. Jeandel, M. Roy-Barman, A new approach to the Nd residence time in the ocean: The role of atmospheric inputs. *Earth Planet. Sci. Lett.* **170**, 433–446 (1999).
31. S. L. Goldstein, R. K. O'Nions, Nd and Sr isotopic relationships in pelagic clays and ferromanganese deposits. *Nature* **292**, 324–327 (1981).
32. S. L. Goldstein, S. R. Hemming, Long-lived isotopic tracers in oceanography, paleoceanography, and ice-sheet dynamics. *Treatise Geochemistry*, **6**, 625 (2003).
33. M. Frank, Radiogenic isotopes: Tracers of past ocean circulation and erosional input. *Rev. Geophys.* **40**, 1–38 (2002).
34. R. L. Rutberg, S. R. Hemming, S. L. Goldstein, Reduced North Atlantic deep water flux to the glacial Southern Ocean inferred from neodymium isotope ratios. *Nature* **405**, 935–938 (2000).
35. A. M. Piotrowski, S. L. Goldstein, S. R. Hemming, R. G. Fairbanks, Temporal relationships of carbon cycling and ocean circulation at glacial boundaries. *Science* **307**, 1933–1938 (2005).
36. A. M. Piotrowski *et al.*, Reconstructing deglacial North and South Atlantic deep water sourcing using foraminiferal Nd isotopes. *Earth Planet. Sci. Lett.* **357–358**, 289–297 (2012).
37. M. Gutjahr, M. Frank, C. H. Stirling, L. D. Keigwin, A. N. Halliday, Tracing the Nd isotope evolution of North Atlantic Deep and Intermediate Waters in the western North Atlantic since the Last Glacial Maximum from Blake Ridge sediments. *Earth Planet. Sci. Lett.* 10.1016/j.epsl.2007.10.037 (2008).
38. F. Lacan, C. Jeandel, Neodymium isotopes as a new tool for quantifying exchange fluxes at the continent-ocean interface. *Earth Planet. Sci. Lett.* **232**, 245–257 (2005).
39. C. Jeandel, T. Arsouze, F. Lacan, P. Téchiné, J. C. Dutay, Isotopic Nd compositions and concentrations of the lithogenic inputs into the ocean: A compilation, with an emphasis on the margins. *Chem. Geol.* **239**, 156–164 (2007).
40. J. N. W. Howe, A. M. Piotrowski, Atlantic deep water provenance decoupled from atmospheric CO_2 concentration during the lukewarm interglacials. *Nat. Commun.* **8**, 1–7 (2017).
41. J. Kim *et al.*, Data from "Nd isotope ratios from DSDP Site 607 in the deep North Atlantic over the last 1.5 Myr, version 1.0.". Interdisciplinary Earth Data Alliance. 10.26022/IEDA/111576 .
42. D. C. Lang *et al.*, Incursions of southern-sourced water into the deep North Atlantic during late Pliocene glacial intensification. *Nat. Geosci.* **9**, 375–379 (2016).
43. A. N. Abbott, B. A. Haley, J. McManus, The impact of sedimentary coatings on the diagenetic Nd flux. *Earth Planet. Sci. Lett.* **449**, 217–227 (2016).
44. J. Du, B. A. Haley, A. C. Mix, M. H. Walczak, S. K. Praetorius, Flushing of the deep Pacific Ocean and the deglacial rise of atmospheric CO_2 concentrations. *Nat. Geosci.* **11**, 749–755 (2018).
45. M. E. Raymo, W. F. Ruddiman, N. J. Shackleton, D. W. Oppo, Evolution of Atlantic-Pacific δ13C gradients over the last 2.5 m.y. *Earth Planet. Sci. Lett.* **97**, 353–368 (1990).
46. M. C. Stordal, G. J. Wasserburg, Neodymium isotopic study of Baffin Bay water: Sources of REE from very old terranes. *Earth Planet. Sci. Lett.* **77**, 259–272 (1986).
47. M. Lambelet *et al.*, Neodymium isotopic composition and concentration in the western North Atlantic Ocean: Results from the GEOTRACES GA02 section. *Geochim. Cosmochim. Acta* **177**, 1–29 (2016).
48. K. A. Refsnider, G. H. Miller, Reorganization of ice sheet flow patterns in Arctic Canada and the mid-Pleistocene transition. *Geophys. Res. Lett.* **37**, 1–5 (2010).
49. N. Zhao *et al.*, Glacial-interglacial Nd isotope variability of North Atlantic Deep Water modulated by North American ice sheet. *Nat. Commun.* **10**, 1–10 (2019).
50. T. Van De Flierdt, M. Frank, D. C. Lee, A. N. Halliday, Glacial weathering and the hafnium isotope composition of seawater. *Earth Planet. Sci. Lett.* **201**, 639–647 (2002).
51. S. R. Hemming, Heinrich events: Massive late Pleistocene detritus layers of the North Atlantic and their global climate imprint. *Rev. Geophys.* **42**, 10.1029/2003RG000128 (2004).
52. W. S. Broecker, T. H. Peng, *Tracers in the Sea* (Eldigio Press, New York, 1982).
53. J. Veizer, Strontium isotopes in seawater through time. *Annu. Rev. Earth Planet. Sci.* **717**, 141–167 (1989).
54. J. D. Blum, "The effect of Late Cenozoic glaciation and tectonic uplift on silicate weathering rates and the Marine 87Sr/86Sr record" in *Tectonic Uplift and Climate Change*, W. F. Ruddiman, Ed. (Springer, 1997), pp. 259–288.
55. R. L. Armstrong, Glacial erosion and the variable isotopic composition of strontium in sea water. *Nat. Phys. Sci (Lond.)* **230**, 132–133 (1971).
56. D. J. DePaolo, Detailed record of the Neogene Sr isotopic evolution of seawater from DSDP Site 590B. *Geology* **14**, 103–106 (1986).
57. M. E. Raymo, W. F. Ruddiman, P. N. Froelich, Influence of late Cenozoic mountain building on ocean geochemical cycles. *Geology* **16**, 649–653 (1988).
58. A. M. Piotrowski *et al.*, Changes in erosion and ocean circulation recorded in the Hf isotopic compositions of North Atlantic and Indian Ocean ferromanganese crusts. *Earth Planet. Sci. Lett.* **181**, 315–325 (2000).
59. K. David, M. Frank, R. K. O'Nions, N. S. Belshaw, J. W. Arden, The Hf isotope composition of global seawater and the evolution of Hf isotopes in the deep Pacific Ocean from Fe-Mn crusts. *Chem. Geol.* **178**, 23–42 (2001).
60. H. F. Ling *et al.*, Evolution of Nd and Pb isotopes in Central Pacific seawater from ferromanganese crusts. *Earth Planet. Sci. Lett.* **146**, 1–12 (1997).
61. R. K. O'Nions, M. Frank, F. Von Blanckenburg, H. F. Ling, Secular variation of Nd and Pb isotopes in ferromanganese crusts from the Atlantic, Indian and Pacific Oceans. *Earth Planet. Sci. Lett.* **155**, 15–28 (1998).
62. J. N. Christensen, A. N. Halliday, L. V. Godfrey, J. R. Hein, D. K. Rea, Climate and ocean dynamics and the lead isotopic records in pacific ferromanganese crusts. *Science* **277**, 913–918 (1997).
63. W. Abouchami, S. L. Goldstein, I. S. J. G. Galer, A. Eisenhauer, A. Mangini, Secular changes of lead and neodymium in central Pacific seawater recorded by a Fe-Mn crust. *Geochim. Cosmochim. Acta* **61**, 3957–3974 (1997).

64. B. C. Reynolds, M. Frank, R. K. O'Nions, Nd- and Pb-isotope time series from Atlantic ferromanganese crusts: Implications for changes in provenance and paleocirculation over the last 8 Myr. *Earth Planet. Sci. Lett.* **173**, 381–396 (1999).
65. M. Frank, R. K. O'Nions, Sources of Pb for Indian Ocean ferromanganese crusts: A record of Himalayan erosion? *Earth Planet. Sci. Lett.* **158**, 121–130 (1998).
66. D. C. Lee *et al.*, Hafnium isotope stratigraphy of ferromanganese crusts. *Science* **285**, 1052–1054 (1999).
67. K. W. Burton, D. Lee, J. N. Christensen, A. N. Halliday, J. R. Hein, Actual timing of neodymium isotopic variations recorded by Fe-Mn crusts in the western North Atlantic. *Earth Planet. Sci. Lett.* **171**, 149–156 (1999).
68. M. Jaume-Seguí *et al.*, Distinguishing glacial AMOC and interglacial non-AMOC Nd isotopic signals in the deep western Atlantic over the last 1 Myr. *Paleoceanogr. Paleoclimatol.* **36**, 1–21 (2021).
69. M. Jaume-Segui *et al.*, Data from "Nd isotope ratios from ODP Site 1063 in the deep western North Atlantic over the last 1.1 Myr, version 1.0." Interdisciplinary Earth Data Alliance. 10.26022/IEDA/111585. Accessed 20 October 2021.
70. J. M. McArthur, R. J. Howarth, G. A. Shields, Strontium isotope stratigraphy. *Geol. Time Scale* **2012**, 127–144 (2012).
71. S. L. Goldstein, R. K. O'Nions, P. J. Hamilton, A Sm-Nd isotopic study of atmospheric dusts and particulates from major river systems. *Earth Planet. Sci. Lett.* **70**, 221–236 (1984).
72. C. G. Bentley, R. H. Thomas, I. Velicogna, "Ice sheets" in *Global Outlook for Ice and Snow* (Department of Earth System Science, University of California, Irvine, 2007), pp. 100–114.
73. E. Rignot, R. H. Thomas, Mass balance of polar ice sheets. *Science* **297**, 1502–1506 (2002).
74. S. L. Bates, M. Siddall, C. Waelbroeck, Hydrographic variations in deep ocean temperature over the mid-Pleistocene transition. *Quat. Sci. Rev.* **88**, 147–158 (2014).
75. P. U. Clark, D. Pollard, Origin of the Middle Pleistocene Transition by ice sheet erosion of regolith. *Paleoceanography* **13**, 1–9 (1998).
76. T. Tanaka *et al.*, JNdi-1: A neodymium isotopic reference in consistency with LaJolla neodymium. *Chem. Geol.* **168**, 279–281 (2000).
77. M. Yehudai *et al.*, Nd isotope ratios from ODP Leg 154, Site 926 in the Deep Equatorial Atlantic over the last 1.5 Myr, version 1.0. Interdisciplinary Earth Data Alliance. 10.26022/IEDA/111588.
78. L. E. Lisiecki, M. E. Raymo, A Pliocene-Pleistocene stack of 57 globally distributed benthic d18O records. *Paleoceanography* **20**, 1–17 (2005).
79. V. Dausmann, M. Frank, M. Gutjahr, J. Rickli, Glacial reduction of AMOC strength and long-term transition in weathering inputs into the Southern Ocean since the mid-Miocene: Evidence from radiogenic Nd and Hf isotopes. *Paleoceanography* **32**, 1–19 (2017).
80. J. McArthur, R. J. Howarth, "Strontium isotope stratigraphy" in *A Geologic Time Scale 2004*, F. M. Gradstein, J. G. Ogg, A. G. Smith, Eds. (Cambridge University Press, 2005), pp. 96–102.
81. M. Frank, B. C. Reynolds, R. Keith O'Nions, Nd and Pb isotopes in Atlantic and Pacific water masses before and after closure of the Panama gateway. *Geology* **27**, 1147–1150 (1999).
82. M. Mudelsee, M. E. Raymo, Slow dynamics of the Northern Hemisphere glaciation. *Paleoceanography* **20**, 10.1029/2005PA001153 (2005).
83. M. A. Maslin, X. S. Li, M. F. Loutre, A. Berger, The contribution of orbital forcing to the progressive intensification of Northern Hemisphere glaciation. *Quat. Sci. Rev.* **17**, 411–426 (1998).
84. J. W. Farrell, S. C. Clemens, L. P. Gromet, Improved chronostratigraphic reference curve of late Neogene seawater 87 Sr/86 Sr. *Geology* **23**, 403–406 (1995).
85. B. Bereiter *et al.*, Revision of the EPICA Dome C CO2 record from 800 to 600-kyr before present. *Geophys. Res. Lett.*, 10.1002/2014GL061957 (2015).
86. J. A. Higgins *et al.*, Atmospheric composition 1 million years ago from blue ice in the Allan Hills, Antarctica. *Proc. Natl. Acad. Sci. U.S.A.* **112**, 6887–6891 (2015).
87. W. F. Ruddiman, M. E. Raymo, D. G. Martinson, B. M. Clement, J. Backman, Pleistocene evolution: Northern Hemisphere ice sheets and North Atlantic Ocean. *Paleoceanography* **4**, 353–412 (1989).
88. J. R. Farmer *et al.*, Deep Atlantic Ocean carbon storage and the rise of 100,000-year glacial cycles. *Nat. Geosci.* **12**, 355–360 (2019).
89. A. Martínez-Garcia *et al.*, Southern Ocean dust-climate coupling over the past four million years. *Nature* **476**, 312–315 (2011).
90. J. R. Farmer *et al.*, Data constraints on ocean-carbon cycle feedbacks at the mid-Pleistocene transition. *Past Glob. Chang. Mag.* **27** (2019).